PNNL-23904

Pacific Northwest
NATIONAL LABORATORY

Proudly Operated by **Battelle** *Since 1965*

Preliminary Phase Field Computational Model Development

Milestone M3: M3CT-14PN0405164

December 2014

Y Li
S Hu
K Xu
JD Suter
JS McCloy
BP Johnson
P Ramuhalli

U.S. DEPARTMENT OF
ENERGY

Prepared for the U.S. Department of Energy
under Contract DE-AC05-76RL01830

DISCLAIMER

This report was prepared as an account of work sponsored by an agency of the United States Government. Neither the United States Government nor any agency thereof, nor Battelle Memorial Institute, nor any of their employees, makes **any warranty, express or implied, or assumes any legal liability or responsibility for the accuracy, completeness, or usefulness of any information, apparatus, product, or process disclosed, or represents that its use would not infringe privately owned rights**. Reference herein to any specific commercial product, process, or service by trade name, trademark, manufacturer, or otherwise does not necessarily constitute or imply its endorsement, recommendation, or favoring by the United States Government or any agency thereof, or Battelle Memorial Institute. The views and opinions of authors expressed herein do not necessarily state or reflect those of the United States Government or any agency thereof.

PACIFIC NORTHWEST NATIONAL LABORATORY
operated by
BATTELLE
for the
UNITED STATES DEPARTMENT OF ENERGY
under Contract DE-AC05-76RL01830

Printed in the United States of America

Available to DOE and DOE contractors from the
Office of Scientific and Technical Information,
P.O. Box 62, Oak Ridge, TN 37831-0062;
ph: (865) 576-8401
fax: (865) 576-5728
email: reports@adonis.osti.gov

Available to the public from the National Technical Information Service,
U.S. Department of Commerce, 5285 Port Royal Rd., Springfield, VA 22161
ph: (800) 553-6847
fax: (703) 605-6900
email: orders@ntis.fedworld.gov
online ordering: http://www.ntis.gov/ordering.htm

This document was printed on recycled paper.
(9/2003)

PNNL-23904

Preliminary Phase Field Computational Model Development

Y Li
S Hu
K Xu
JD Suter
JS McCloy
BP Johnson
P Ramuhalli

December 2014

Prepared for
the U.S. Department of Energy
under Contract DE-AC05-76RL01830

Pacific Northwest National Laboratory
Richland, Washington 99352

Summary

This report presents progress towards the development of meso-scale models of magnetic behavior that incorporate microstructural information as an effort to create computational tools to ultimately assess material integrity. Radiation-induced defects will cause microstructural changes that can be assessed using domain wall motion. However, modeling magnetic signatures in irradiated materials with complex microstructures (such as structural steels) is a significant challenge. The complexity is addressed incrementally, using monocrystalline Fe (i.e., ferrite) films as model systems to develop and validate initial models, followed by polycrystalline Fe films, and then by more complicated and representative alloys. In addition, the modeling will ultimately address the inclusion of other major phases (e.g., martensite, austenite), minor magnetic phases (e.g., carbides, FeCr precipitates), and minor nonmagnetic phases (e.g., Cu precipitates, voids).

The focus of the magnetic modeling is on phase-field models based on the numerical solution to the Landau-Lifshitz-Gilbert equation. From a computational standpoint, phase-field modeling allows the simulation of large enough systems that relevant defect structures and their effects on functional properties, such as magnetism, can be simulated.

To date, two phase-field models have been generated in support of this work. First, a bulk iron model with periodic boundary conditions was generated as a proof-of-concept to investigate major loop effects of single versus polycrystalline bulk iron and effects of single non-magnetic defects. More recently, to support the experimental program herein using Fe thin films, a new model was generated that uses finite boundary conditions representing surfaces and edges. This model has provided key insights into the domain structures observed in magnetic force microscopy (MFM) measurements. Simulation results for single crystal thin-film iron indicate the feasibility of the model for determining magnetic domain wall thickness and mobility in an externally applied field. Because the phase-field model dimensions are limited relative to the size of most specimens used in experiments, special experimental methods were devised to create similar boundary conditions in the iron films. Preliminary MFM studies conducted on single and polycrystalline iron films with small sub-areas created with focused ion beam have correlated quite well with phase-field simulations. However, phase-field model dimensions are still small relative to experiments thus far. We are in the process of increasing the size of the models and decreasing specimen size so that in the future both will have the same dimensions.

Ongoing research is focused on validation of the phase-field models and is being accomplished through comparison with experimentally obtained MFM images (in progress), and planned measurements of major hysteresis loops and first order reversal curves.

Acronyms and Abbreviations

Code	ASME Boiler and Pressure Vessel Code
DW	domain wall
EBSD	electron backscatter diffraction
EDS	energy dispersive spectroscopy
FFT	fast Fourier transform
FIB	focused ion beam
FORC	first order reversal curve
ISI	in-service inspection
LLG	Landau–Lifshitz–Gilbert
MBN	magnetic Barkhausen noise
MFM	magnetic force microscopy
NDE	nondestructive evaluation
SEM	scanning electron microscopy
SSC	structures, systems, and components
VSM	vibrating sample magnetometer

Contents

Summary iii
Acronyms and Abbreviations v
1.0 Introduction 1.1
  1.1 Motivation 1.1
  1.2 Magnetic Signatures of Nuclear Structural Materials Degradation 1.2
  1.3 Magnetic Measurements for Multi-scale NDE Proof-of-Concept 1.3
  1.4 Meso-scale Models 1.4
  1.5 Organization of Report 1.5
2.0 Phase Field Modeling: Theory and Application 2.1
  2.1 Introduction of Magnetism 2.1
  2.2 Landau–Lifshitz–Gilbert Equation 2.2
  2.3 Numerical Solution of LLG Equation 2.4
  2.4 Extracting Domain Wall Parameters 2.5
  2.5 Relation between Magnetic Measurements and Modeling 2.5
  2.6 Modeling of Complexity 2.6
    2.6.1 Domain Wall Motion 2.6
    2.6.2 Effect of Grain Boundaries in Bi-crystalline Fe 2.6
    2.6.3 Effect of Inclusions 2.6
    2.6.4 Effect of Dislocations 2.7
3.0 Results 3.1
  3.1 Magnetic Domain Morphologies of Single-Crystal Thin Film 3.1
  3.2 Magnetic Domain Wall Thickness 3.3
  3.3 Magnetic Domain Switching with Applied Magnetic Field 3.4
  3.4 Experimental Set-up for MFM 3.8
  3.5 MFM and Modeling Comparisons for Single Crystal Film Fe 3.9
  3.6 MFM of Polycrystalline Film Fe 3.11
4.0 Conclusions and Future Work 4.1
5.0 References 5.1

Figures

2.1 (a) Magnetic Hysteresis Loop of a Single Crystal Iron. (b) Snapshots of Magnetic Domain Morphologies of the Central x_1x_2 Plane at the Labeled Points of (a). 2.2

3.1 Initial and Equilibrium Magnetic Domain Structures Obtained in a Free-standing α-Fe Film 3.1

3.2 Comparison of Film Thickness Effect on Ferromagnetic Domain Structures 3.2

3.3 Comparison of Film Size Effect on Magnetic Domain Structures 3.3

3.4 Magnetization Varies Along the Lines AA’ and BB’ of Figure 3.3 .... 3.4

3.5 Magnetic Domain Switching with Applied Magnetic Field 3.6

3.6 Magnetic Domain Switching with Applied Magnetic Field 3.7

3.7 Magnetic Domain Switching with Applied Magnetic Field 3.8

3.8 SEM Showing FIB-milled Rectangular “Island” in Single-crystal Fe Film 3.9

3.9 MFM Images as a Function of Applied Field for the 5 × 10 µm FIB Region of Single Crystal Fe 3.10

3.10 Phase-Field Simulation of Rectangular Aspect Ratio Fe Films 3.10

3.11 Phase-Field Simulation of Square Aspect Ratio Fe Thin Film and Measured MFM Image 3.11

3.12 MFM and Corresponding EBSD Image of Thin Film Polycrystalline Fe at the Same Scale 3.12

3.13 EBSD Image of Portion of the Polycrystalline Iron Film, with the Large Black Square Indicating the ~100-µm Scribed Area 3.12

Tables

2.1 Material Properties of α-iron (Fe) Used in the Simulations 2.5

1.0 Introduction

1.1 Motivation

The research described in this report is part of a greater effort to integrate microstructural metrology, micro-magnetic measurements, and meso-scale phase-field modeling to develop advanced tools and techniques that can extract semi-quantitative diagnostic and interpretive information about the state of microstructural damage in a material based on magnetic signature data alone. This technology has potential for maturation into a real-time, in-situ monitoring capability for structural materials.

Advanced materials characterization techniques and tools are needed to enable a comprehensive understanding of nuclear structural material changes when exposed to high temperatures and radiation environments. Improving the understanding of nuclear structural materials in these extreme environments is critical to the development of structural monitoring technologies for monitoring the health of structures, systems, and components (SSCs) to ensure continued safe operation of nuclear power facilities. The need for effective and reliable monitoring of structural health is not limited to the current fleet; rather, the anticipated higher temperatures and fluences in advanced reactor designs are expected to exacerbate the need for such technologies.

In-service inspection (ISI) technologies based on nondestructive evaluation (NDE) for detecting and characterizing cracking and other forms of degradation are widely used in operating nuclear power plants. Acceptable techniques and acceptance criteria for cracking in pressure boundary components are defined in the ASME Boiler and Pressure Vessel Code (“Code”) and incorporated into regulatory guidance by reference in the Code of Federal Regulations.

ISI using Code-accepted NDE techniques is one element of the defense-in-depth philosophy that has guided the regulation and operation of these plants and has been generally successful in the detection of cracking. However, accepted technologies are limited in that they are primarily focused on the detection of cracking or metal loss. This has two drawbacks. First, as plants age, and as advanced reactor technologies are developed, alternative degradation mechanisms such as irradiation embrittlement are expected to be of equal or greater importance to the safety and economics of nuclear power plant operation. Second, the detection of degradation needs to take place at earlier stages in the degradation lifecycle, to enable appropriate mitigation actions. The applicability of Code-accepted NDE techniques to degradation mechanisms such as irradiation embrittlement is not clear, and alternative methods for detecting such degradation early in its lifecycle are needed.

Meeting this need will require improving the fundamental understanding and diagnostic characterization of reactor structural materials. One essential piece of this sizable challenge includes developing characterization tools and integrating them with simulation models that are based on first-principles. In order to detect early stages of material degradation, and reduce operational uncertainty, these models will need to be able to relate the onset of irradiation-induced material degradation phenomena at the meso-scale (defined as 10’s of nm to 100’s of µm) to degradation signatures that can be effectively monitored via in-service NDE.

1.2 Magnetic Signatures of Nuclear Structural Materials Degradation

The majority of the structural components used in light-water reactors are fabricated from various Fe-Cr-Ni alloys, such as carbon steels (e.g., A553B), stainless steels (e.g., 304 and 308), and nickel-based alloys (e.g., Alloy 600 and X750) and the corresponding weld materials used to join them. In general, these materials have exhibited excellent performance in high temperature and pressurized water and steam systems. However, the unique combination of high temperatures, high pressure, aqueous exposure, and neutron flux creates a very harsh environment and activates material degradation processes that can reduce the capacity of these components to perform within their desired operating and safety envelope. Correspondingly, materials for new reactors will likely include high-temperature radiation-tolerant materials such as high-chromium steels and oxide dispersion strengthened steels (Zinkle and Busby 2009).

Typical irradiation-induced degradation mechanisms in nuclear reactor structural materials include corrosion, embrittlement, cracking, and swelling, and mechanisms that are strongly related to microstructural changes. The latter include second phase precipitation/dissolution, defect cluster formation, and void evolution, and affect mechanical properties as well as other physical properties (such as magnetic and electrical properties).

Magnetic signatures provide a unique and powerful ability to both evaluate changes in bulk ferromagnetic material properties and to correlate those changes to microstructural features. Research has shown correlations between changes in microstructure, mechanical properties, and magnetic properties. For example, NDE measurements of steels show a correlation between neutron irradiation hardening and changes in bulk magnetic signatures (Park et al. 1997). Recent investigations demonstrate the possibility to correlate magnetic NDE data sets (e.g., Barkhausen noise) to micro-magnetic properties resulting from microstructural features of the material (Henager Jr. et al. 2013). For example, irradiation-induced formation of Cr precipitates in Fe-Cr-Ni steels was observed to result in changes to bulk magnetic NDE signatures [e.g., major (Kamada et al. 2013) and minor (Kobayashi et al. 2012a) hysteresis loops] and changes in hardness. Additionally, recent work has shown irradiation-induced magnetic changes in A508 ferritic steels (Kempf et al. 2014), Fe-1wt%Cu alloys (Lo 2012), and even nominally non-magnetic austenitic alloys (Gussev et al. 2014). Meso-scale magnetic imaging techniques (e.g., magnetic force microscopy, or MFM) are able to measure changes in magnetic domain wall (DW) mobility from different microstructural features (Takaya et al. 2004; Batista et al. 2013). The use of bulk magnetic measurements in predictive estimates of damage and remaining life has also been recently demonstrated (Ramuhalli et al. 2012). Thus, magnetic signatures, with the appropriate tools that enable extraction of quantitative diagnostic information, may allow meaningful correlation of irradiation-induced microstructural changes to measurable bulk material changes. Because magnetic measurements can be made nondestructively over several orders of magnitude in length scales, this signature also has great potential to be used to verify and validate robust, physics-based, meso-scale computational models that incorporate microstructure, chemistry, and mechanical and magnetic properties.

Because each of the materials used or planned for use in reactor pressure vessels and pressure boundary components contains at least minor magnetic components, we hypothesize that irradiation-induced defects in metallic structural materials will cause changes in the microstructure that produce variation in DW mobility and, hence, in their magnetic properties. Measuring changes in DW mobility should therefore help determine the state of damage in these materials. To accomplish this, meso-scale modeling will need to be coupled with micro-property magnetic measurements, microstructural characterization, and material testing to obtain *quantitative correlations* between variations in DW mobility, microstructural features, and material properties as a result of degradation. Ultimately, this knowledge can inform improved bulk-scale magnetic NDE techniques for quantifying irradiation-induced degradation of materials in the field based on key magnetic signatures.

By coupling magnetic imaging capabilities with classical analytical microscopy methods, such as scanning electron microscopy (SEM), electron back scatter diffraction (EBSD), and energy dispersive spectroscopy (EDS), it is now possible to construct meso-scale structure, chemistry, crystallography, and magnetic property information that can be used to identify important relationships between microstructure evolution and material response. Recent work (Batista et al. 2012) demonstrated combined EBSD and MFM on ferrite/cementite steels for studying detailed mechanisms of second phase formation. The authors of the present work have also looked at correlations between MFM and EBSD in reactor materials such as HT-9 (Henager Jr. et al. 2013). The present work is examining similar correlations in irradiated and non-irradiated thin films to gain a fundamental understanding of the impact of irradiation on magnetic signatures.

1.3 Magnetic Measurements for Multi-scale NDE Proof-of-Concept

By using magnetic phenomenology, a suite of techniques can be used together to explore the effect of defects, as those created by irradiation, on NDE measurements to be ultimately used in online condition monitoring. The goal is to use Barkhausen noise emission as the NDE method. It has been shown many times that mechanical changes in steels, such as those resulting from neutron irradiation, have effects on Barkhausen noise (e.g., Sipahi et al. 1994; Park et al. 1999a; Park et al. 1999b; Altpeter et al. 2001; Chang et al. 2002) and the major loops of magnetization (e.g., Park et al. 1997; Park et al. 2003; Park et al. 2004). Therefore major hysteresis loops, such as those obtained with a vibrating sample magnetometer (VSM) where magnetization is saturated at positive and negative field values, should be obtained on laboratory specimens. These measurements provide magnetic coercivity (or "magnetic hardness"), which has many times been shown to correlate with mechanical hardness, because of the same defects preventing both plastic deformation and magnetic domain wall movement. More detailed micromagnetic information about magnetic switching can be obtained from other magnetic field dependent measurements, such as minor loops, where the applied magnetic field magnitude is too small to reach positive or negative saturations. Minor loop characteristics have been shown to relate to neutron damage in steels (Takahashi et al. 2006; Kobayashi et al. 2009; Kobayashi et al. 2012b). Finally, first order reversal curves (FORCs) are similar to minor loops but consist of only part of the loop. Each FORC is obtained by 1) saturating at a positive field, 2) ramping down to a reversal field H_r, measuring magnetization M at increasing fields H starting from H_r. The FORC function for FORCs taken after saturation at a positive field is then defined as (Mayergoyz 1991; Newell 2005): $\rho(H_r,H) = -\frac{1}{2}\frac{\partial^2 M(H_r,H)}{\partial H_r \partial H}$. A polynomial fit is created to this surface then allows extraction of various parameters that describe the switching field distribution of coercivity, rather than a single value as in the case of the major loop (Winklhofer and Zimanyi 2006).

We have recently shown that parameters extracted from a FORC diagram, which contains detailed information about magnetic switching and hence defect structure, are linearly related to NDE signatures extracted by magnetic Barkhausen noise measurements (Henager Jr. et al. 2013). We thus aim to show correlations from the most abstracted scale of Barkhausen noise, down through the laboratory measurements taken by VSM, including major loop hysteresis, minor loops, and FORCs, to *ultimately focus on the defect interactions with the magnetic domain walls taking place at the microstructural and nano-structural level*. To visualize these interactions, we take a dual experimental-computational approach. The experiments and computational models then also permit cross-validation, with experimental parameters seeding models and the computational models assisting in interpretation of experimental magnetic images.

Experimentally, magnetic force microscopy (MFM) is used to investigate the behavior of magnetic domain walls as they propagate in the presence of an applied magnetic field and encounter various defects such as dislocations, grain boundaries, and second phase particles (voids or precipitates). In addition to providing visualization of interaction of magnetic domain walls with defects, quantitative information is obtainable from MFM as well. MFM resolution is typically 25–50 nm depending on tip configuration, and magnetic domain walls in iron on are on this order or larger (Lau and Shaw 2011). Theoretically, pixel-by-pixel magnetic hysteresis curves can be generated by quantitatively analyzing MFM data (Babcock et al. 1996; Sorop et al. 2003; Zhu et al. 2003). Thus magnetic imaging methods such as MFM provide a critical experimental tool to obtain numerical parameters (such as de-pinning fields, domain wall mobilities, etc.) for domain wall dynamics, as affected by defects, which can be put into microstructural models of magnetic materials to study the evolution of magnetic signatures as a function of changes of defect concentration and magnetic field.

1.4 Meso-scale Models

This interim report presents progress towards the development of meso-scale models of magnetic behavior that incorporate microstructural information. Modeling magnetic signatures in irradiated materials with complex microstructures (such as structural steels) will represent a significant but necessary challenge. The complexity will be addressed incrementally, using the monocrystalline Fe (i.e., ferrite) film as model-systems to develop and validate initial models, followed by polycrystalline Fe films, and by more complicated and representative alloys. Additional microstructure complexity factors that will be addressed include effect of crystal orientation, grain boundaries, voids, and minor nonmagnetic inclusions (e.g., Cu precipitates).

The focus of the modeling is on phase-field models. Phase-field models of magnetic domain evolution enable the study of the effect of individual defects, such as magnetic particles or dislocations on magnetic domain nucleation, DW mobility, and magnetic response (Hu et al. 2013). An important advantage of phase-field modeling techniques is that they can be done at time and length scales that can be experimentally verified using micro-magnetic imaging techniques such as MFM and SEM. These simulations generate microstructure-property data, such as hysteresis loop and first order reversal curve (FORC) data (McCloy et al. 2013). FORC essentially maps a distribution of magnetic coercivities that can be assigned to multiple magnetic phases or defects, and the effect of simulated defects can be explored with these FORC diagrams. Experiments have shown that FORC data is closely correlated to hardness and bulk NDE data collected using magnetic Barkhausen noise (MBN) methods (applicable to ~m^2 samples) (Henager Jr. et al. 2013). Therefore, modeling with experimental validation can provide insight into microstructural behavior, material properties, and NDE signal physics. The results from phase field models can be used to interpret micro-magnetic property data, and to estimate the state of microstructural damage from magnetic measurements.

From the computational standpoint, phase-field modeling allows the simulation of large enough systems that relevant defect structures and their effects on functional properties like magnetism can be simulated. To date, two phase field models have been generated in support of this work. First, a bulk iron model with periodic boundary conditions was generated as a proof-of-concept to investigate major loop effects of single versus polycrystalline bulk iron (Henager Jr. et al. 2013) and effects of single non-magnetic defects (Hu et al. 2013). More recently, to support the experimental program herein using iron thin films, a new model was generated that uses finite boundary conditions representing surfaces and edges (see Section 2.0 in this report). This model will be key to understanding the domain structures observed in MFM measurements. Because the phase field modeling is limited to spatial domains of small size (usually 10s of nm to a few microns on each side), special experimental methods are needed to create similar boundary conditions in the iron films.

1.5 Organization of Report

The rest of this report is organized as follows. Section 2 briefly discusses the physics of magnetism that are incorporated in phase field models, and describes the model itself. Section 3 presents examples of results from the model, specifically focused on DW configurations in thin-films in the presence of an external magnetic field. Section 4 presents conclusions based on the data available to date, and describes ongoing work in this area.

2.0 Phase Field Modeling: Theory and Application

2.1 Introduction of Magnetism

A magnetic domain is a region within a magnetic material that has uniform magnetization. This means that the individual magnetic moments of the atoms are aligned with one another and they point in the same direction. A domain wall is a narrow transition region at the boundary between adjacent magnetic domains, over which the magnetization direction changes from one domain to the next. Domain walls in magnetic materials are categorized based on the plane of rotation of the magnetization as it transitions across the domain wall. In a Bloch domain wall the magnetization rotates through the plane of the domain wall, while in Néel walls, the magnetization rotates from the direction of the first domain to the direction of the second, with a rotation that is within the plane of the domain wall. Both the 360° domain wall and 180° domain wall illustrated in Figure 2.1(c) are Bloch domain walls.

The domain wall itself can move when an external magnetic field is applied. Figure 2.1(b) shows the movement of 180° domain walls with an external field. The domain with magnetizations along the applied field direction grows while the domain with magnetization opposite to the applied field shrinks.

Hysteresis has been one of the most enduring representations of magnetic domain behavior (Bertotti 1998), and is related to domain wall movement by relating the external magnetic force required to create movement in domain boundaries. Figure 2.1(a) displays a typical hysteresis loop. It was from a simulation of single iron crystal with a 360° domain wall (Hu et al. 2013), meaning that the magnetic domain vector rotates a full 360 across the wall. The magnetic domain morphologies at the points listed in the hysteresis loop of Figure 2.1(a) are illustrated in Figure 2.1(b). The hysteresis loop started from point (A) where multiple domains coexist as shown in Figure 2.1(b)(A). When the applied magnetic field H_{ex1} reached its maximum, a 360° domain wall was formed and remained (see Figure 2.1(b)(B)). At this point, the magnetic domain vectors (represented by black arrows) all point the same direction, in alignment with (and parallel to) the applied field. When unloading (i.e., decreasing the field), the 360° domain wall thickened as shown by Figure 2.1(b)(C). When the applied magnetic field H_{ex1} switched its direction, an anti-direction domain of $(-M_s,0,0)$ nucleated in the center of the simulation cell and grew by splitting the 360° domain wall into two 180° domain walls. From Figure 2.1(b)(B) to Figure 2.1(b)(H), it is seen that a process of emerging and splitting of a 360° domain wall occurred repeatedly during the domain switching. Consequently, the corresponding hysteresis loop is repeatable.

In Figure 2.1(a), the applied magnetic field H_{ex1} is along the x_1-direction. Its values at points (D) and (G) are called the coercive field, H_c. The plotted hysteresis loop uses the average magnetization $\mathbf{M} = \left(M_1, M_2, M_3\right)$ along the x_1-direction; that is, $\bar{M}_1$ versus H_{ex1}. The corresponding magnetization at point (C) and (F) are called the remanent magnetization. M_s is the saturation magnetization of the magnetic material.

Figure 2.1. (a) Magnetic Hysteresis Loop of a Single Crystal Iron. (b) Snapshots of Magnetic Domain Morphologies of the Central x_1x_2 Plane at the Labeled Points of (a). The outside box is the 3-D simulation cell, the black arrows are the magnified magnetization vectors shown in the corresponding domains, and the color illustrates the magnitude of the magnetization component M_3^* as depicted by the color bar (e.g., blue is into the page indicated as ⊗ and red is out of the page indicated as ⊙), where M_3^* is related to the magnetization vector M as $\mathbf{M} = M_s\mathbf{M}^* = M_s\left(M_1^*, M_2^*, M_3^*\right)$. (c) Arrowed Bloch domain walls at the given points (E, F, G). (E) represents a 360° wall, (F) shows two split 180° walls, and (G) shows a single 180° wall (Hu et al. 2013).

2.2 Landau–Lifshitz–Gilbert Equation

Magnetization changes direction thus domain switching with applied magnetic field can be described by the well-known Landau–Lifshitz–Gilbert (LLG) equation. The LLG equation has the form of (Hubert and Schaefer 1998; Gilbert 2004; Zhang and Chen 2005; Hu et al. 2013)

$$\left(1+\alpha^2\right)\frac{\partial \mathbf{M}}{\partial t} = -\gamma_0 \mathbf{M}\times\mathbf{H}_{eff} - \frac{\gamma_0\alpha}{M_s}\mathbf{M}\times\left(\mathbf{M}\times\mathbf{H}_{eff}\right), \tag{2.1}$$

where M_s is the saturation magnetization of the magnetic phase as stated above, γ_0 is the corresponding gyromagnetic ratio, α is the dimensionless damping constant, and $\mathbf{H}_{eff}$ is the effective magnetic field, which can be represented as a variational derivative of the total free energy F of the system with respect to magnetization,

$$\mathbf{H}_{eff} = -\frac{1}{\mu_0}\frac{\delta F}{\delta \mathbf{M}}, \tag{2.2}$$

where $\mu_0 = 4\pi\times10^{-7}$ NA^{-2} is the permeability of vacuum. The magnetization vector, $\mathbf{M}(\mathbf{x},t)$, is a function of space and time, describing the magnetization spatial inhomogeneity and varying with time where $\mathbf{x}=(x_1,x_2,x_3)$ is a global coordinate and t is time. The total free energy includes magnetocrystalline anisotropy energy (F_{anis}), exchange energy (F_{exch}), magnetostatic energy (F_{magn}), magnetic external field energy (F_{extr}), and elastic energy (F_{elas}),

$$F = F_{anis} + F_{exch} + F_{magn} + F_{extr} + F_{elas}\,. \tag{2.3}$$

All energy terms in Eq. (2.3) depend on the magnetization distribution in the magnet considered. By taking $\mathbf{M} = M_s\mathbf{M}^* = M_s\left(M_1^*, M_2^*, M_3^*\right)$, the magnetocrystalline anisotropic energy in a cubic anisotropic magnet can be expanded in term of magnetization components as:

$$F_{anis} = \int_V \left[K_1\left(M_1^{*2}M_2^{*2} + M_1^{*2}M_3^{*2} + M_2^{*2}M_3^{*2}\right) + K_2 M_1^{*2}M_2^{*2}M_3^{*2}\right]dV\ , \tag{2.4}$$

where K_1 and K_2 are the anisotropy constants. They are the intrinsic material properties and have values in the range of $\pm10^4$ J/m^3.

The exchange energy is calculated through the gradients of the magnetic components as

$$F_{exch} = \int_V A_c\left[\left(\nabla M_1^*\right)^2 + \left(\nabla M_2^*\right)^2 + \left(\nabla M_3^*\right)^2\right]dV\ , \tag{2.5}$$

where A_c is the exchange stiffness constant and $\nabla M_i^* = \left(\frac{\partial M_i^*}{\partial x_1}, \frac{\partial M_i^*}{\partial x_2}, \frac{\partial M_i^*}{\partial x_3}\right)$.

The magnetostatic energy is of the form

$$F_{magn} = -\frac{1}{2}\mu_0\int_V \mathbf{H}_{ex}\cdot\mathbf{M}\,dV \tag{2.6}$$

where $\mathbf{H}_d = \left(H_{d1}, H_{d2}, H_{d3}\right)$ is the stray field and governed by

$$H_{d1,1} + H_{d2,2} + H_{d3,3} = -M_s\left(M_{1,1}^* + M_{2,2}^* + M_{3,3}^*\right),\ \nabla\times\mathbf{H}_d = 0\,. \tag{2.7}$$

If an external magnetic field $\mathbf{H}_{ex} = \left(H_{ex1}, H_{ex2}, H_{ex3}\right)$ is applied, the corresponding energy density can be obtained by

$$F_{extr} = -\mu_0\int_V \mathbf{H}_{ex}\cdot\mathbf{M}\,dV\ . \tag{2.8}$$

A magnetic body will deform under the influence a magnetic interaction. The deformation can be described by the spontaneous or stress-free strain tensor, ε_{ij}^{0}, due to the presence of magnetization:

$$\varepsilon_{ii}^{0} = \frac{3}{2}\lambda_{100}\left(M_i^{*2} - \frac{1}{3}\right),\ \varepsilon_{ij}^{0} = \frac{3}{2}\lambda_{111}M_i^{*}M_j^{*},\ \ i \neq j\,, \tag{2.9}$$

where λ_{100} and λ_{111} are the magnetostrictive constants. The corresponding elastic energy density is

$$f_{elas} = \frac{1}{2}c_{ijkl}e_{ij}e_{kl} = \frac{1}{2}c_{ijkl}\left(\varepsilon_{ij} - \varepsilon_{ij}^{0}\right)\left(\varepsilon_{kl} - \varepsilon_{kl}^{0}\right), \tag{2.10}$$

where e_{ij} and ε_{ij} are the elastic strain and total strain, respectively. c_{ijkl} is the elastic constant tensor. The strains ε_{ij} can be obtained by solving

$$\sigma_{ij} = c_{ijkl}\left(\varepsilon_{kl} - \varepsilon_{kl}^{0}\right), \sigma_{ij,j} = 0, \varepsilon_{ij} = 1/2\left(u_{i,j} + u_{j,i}\right), i, j = 1,2,3 \tag{2.11}$$

under given boundary condition, where u_i is the displacement component and σ_{ij} is the stress component.

In order to numerically calculate these energies, we need to know the anisotropic energy coefficients (K_1, K_2), the exchange stiffness constant (A_c), the magnetostrictive constants (λ_{100}, λ_{111}), and the elastic stiffness tensor (c_{ijkl}). They are all intrinsic material properties and are available for most common magnetic materials (Bertotti 1998).

2.3 Numerical Solution of LLG Equation

By solving Eq. (2.1), we can obtain how $\mathbf{M}(\mathbf{x},t)$ varying with space point $\mathbf{x}$ and time t, and can thus obtain the magnetic domain structure distribution and its changes with time. In general, there is no analytical solution for Eq. (2.1), and the equation has to be solved numerically. We employ a fractional step procedure and Gauss–Seidel approach (Wang et al. 2001) and fast Fourier transform (FFT) (Zhang and Chen 2005) to numerically solve Eq. (2.1). Details can be found in Wang et al. (2001) and Zhang and Chen (2005) and the interested reader is referred to these.

In this study, we have numerically solved Eq. (2.1) using a series implementation of the numerical solution with a spatial size of $128l_0 \times 128l_0 \times 64l_0$ or $96l_0 \times 192l_0 \times 64l_0$ uniform grids where l_0 is the grid length. Periodic boundary conditions are used in all three spatial directions in order to use FFT. We assume that the model material is body-centered cubic α-phase iron with material constants listed in Table 2.1. For the purposes of the simulation, we chose l_0=10 nm. This choice was based on the results of a parametric simulation study around the parameter l_0, which indicated that choosing this parameter to be much larger would negatively impact the convergence of the model.

A parallel version of this implementation has been also developed for simulating magnetic domain structure in a bulk material with a larger size and is being tested to verify the implementation.

Table 2.1. Material Properties of α-iron (Fe) Used in the Simulations

Symbol	Units	Value	Refs
α	Unitless	0.05	
M_s	Am^{-1}	1.71×10^6	Craik (1995)
$\mu_0 M_s$	$NA^{-1}m^{-1}$	2.15	d'Aquino (2004)
K_1	J/m^3	4.80×10^4	Cullity and Graham (2009)
K_2	J/m^3	5.0×10^3	Cullity and Graham (2009)
A_c	J/m	1.5×10^{-11}	Bertotti (1998)
$(\gamma_0 M_s)^{-1}$	ps (picosecond)	2.6	d'Aquino (2004)
λ_{100}	Unitless	2.10×10^{-5}	Cullity and Graham (2009)
λ_{111}	Unitless	1.57×10^{-5}	Cullity and Graham (2009)
C_{11}	GPa	230	Adams et al. (2006)
C_{12}	GPa	134	Adams et al. (2006)
C_{44}	GPa	116	Adams et al. (2006)

where C_{ij} is the elastic stiffness in the Voigt notation.

2.4 Extracting Domain Wall Parameters

Equation (2.1) is a dynamic equation so the magnetization vector **M** at each spatial point **x** changes with time t in the presence of an applied field. Therefore, the corresponding domains and domain walls move with time. The mobility of domain wall motion depends on the gyromagnetic ratio (γ_0), the damping constant (α), and the change rate of applied magnetic field. Experimentally, the vibrating sample magnetometer (VSM) is able to measure the mobility. The numerical simulations simulate domain wall motion, though formal methods of extracting and quantifying mobility from the simulations are needed.

A second parameter of interest is the domain wall width or thickness. As stated earlier, a domain wall forms a continuous transition between two magnetic domains. For this reason there can be no unique definition of a domain wall width. A discussion of domain wall width can be found in Hubert and Schaefer (1998). For our numerical simulations, we use at least three grid points within the magnetization transition region in order to avoid numerical pinning or inaccuracy.

2.5 Relation between Magnetic Measurements and Modeling

Common magnetic measurement techniques include MFM and VSM, with the MFM used to measure magnetic domain structure while the VSM used to measure hysteresis loops. The simulations, as stated earlier, use the LLG equation to extract magnetic domain structure, mobility, and the hysteresis loop. As a result, the domain structure morphologies from MFM and the hysteresis loops from VSM may be used to validate the models. Note that the validation process will still require knowledge of fundamental parameters (such as the gyromagnetic ratio) for input to the model. However, it is likely that the measured MFM and VSM data may be used, along with the model, to compute best fits to these parameters. Such inverse analysis has not been attempted in this study to date.

2.6 Modeling of Complexity

Currently, the simulation model is developed for single-crystal thin film with its edges parallel to the magnetization easy axes. The model can be modified to simulate a single crystal with an arbitrary orientation by introducing a local coordinate and coordinate transformation matrix, or some precipitates or holes by employing phase-field order parameters. The model may also be extended to simulate polycrystalline films with or without extra defects such as precipitates and dislocations.

The incorporation of complexity into the model is performed in a staged manner, with the inclusion of polycrystalline materials (with grain boundaries), inclusions, and dislocations.

2.6.1 Domain Wall Motion

Domain walls can move when external magnetic field is applied and the field is larger than the critical magnitude needed to initiate the domain wall movement. The domain walls move in such a way as to increase the size of the domains of same/similar direction as the applied field and in such a way as to reduce the size of domains of opposite direction as the applied field.

Because the magnetization favors to align with the magnetic easy axes, the orientations of the domains formed in a grain depend on the orientation of the grain. Thus, the domain wall movement also depends on the grain orientation in addition to the applied field magnitude and direction.

2.6.2 Effect of Grain Boundaries in Bi-crystalline Fe

Because the grain orientation affects the magnetization directions, the response of a bi-crystal to an applied magnetic field will be different when the bi-crystal has a low and high angle grain boundary. A bi-crystal with a low angle grain boundary behaves similarly to a single crystal. But a bi-crystal with a large angle grain boundary could show significant difference. For example, a bi-crystal with a large angle grain boundary may result in a smaller remnant magnetization and a smaller coercive field comparing a single crystal piece.

The main effect of triple points or multiple grain boundaries is through the difference in the orientations around the triple joints or grain boundaries. These points or regions may pin domain wall movement or initiate new domain nucleation during domain switching.

2.6.3 Effect of Inclusions

Inclusions such as precipitates or holes/pores also affect the response of a Fe crystal to an applied field. They always behave as domain wall movement pinners and nucleation sites of new domains during domain switching. Therefore, they could cause magnetic hardening or softening (changes in magnetic coercivity) depending on the dominant role of either pinning or nucleation sites they play. Their roles are closely correlated to their sizes.

2.6.4 Effect of Dislocations

Dislocations also have effects of the magnetism of Fe crystals. The coercive field of a Fe crystal is proportional to the square root of the dislocation density inside the crystal. That means that dislocations always cause magnetic hardening.

3.0 Results

3.1 Magnetic Domain Morphologies of Single-Crystal Thin Film

Consider a single-crystal film of body-centered cubic α-phase iron. The corresponding material constants are listed in Table 2.1. Because the magnetostrictive constants are relatively small, the elastic interaction energy is ignored for the following simulations. All simulations are run with a series code in a simulation cell of $128l_0 \times 128l_0 \times 64l_0$ or $96l_0 \times 192l_0 \times 64l_0$ uniform grids where l_0=10 nm.

In order to predict the magnetic domain morphology in a freestanding iron thin film, a spatially dependent order parameter, η_0, is introduced to distinguish a film by changing its value from 1 to 0. $\eta_0=1$ refers to the film body, $\eta_0=0$ refers to outside of the film. Therefore, $\mathbf{M}^*=\eta_0\mathbf{m}=\eta_0(m_1,m_2,m_3)$ and $|\mathbf{m}|=1$ can distinguish the magnitude of $\mathbf{M}^*$ inside and outside of the film. Without any applied field, the magnetic domain structure at equilibrium state is shown in Figure 3.1(b). The simulation starts from a random distribution of magnetization as shown in Figure 3.1(a) and stops when the magnetic domains reach an equilibrium state. The equilibrium state means that the domain structure does not change with time anymore. It is seen that the magnetization vector near the film surface is always parallel to the film surface and forms a vortex domain shape with the head-to-tail magnetization configuration across a domain wall, which minimizes the magnetostatic energy. For this square-shaped simulation cell, this configuration generates 90° domain walls that start at the corners and meet in the center, essentially drawing diagonal lines across the surface. The effect of the film thickness on magnetic domain structures is illustrated in Figure 3.2. It is clearly shown that the film thickness does not alter the domain structure with the considered thickness variance.

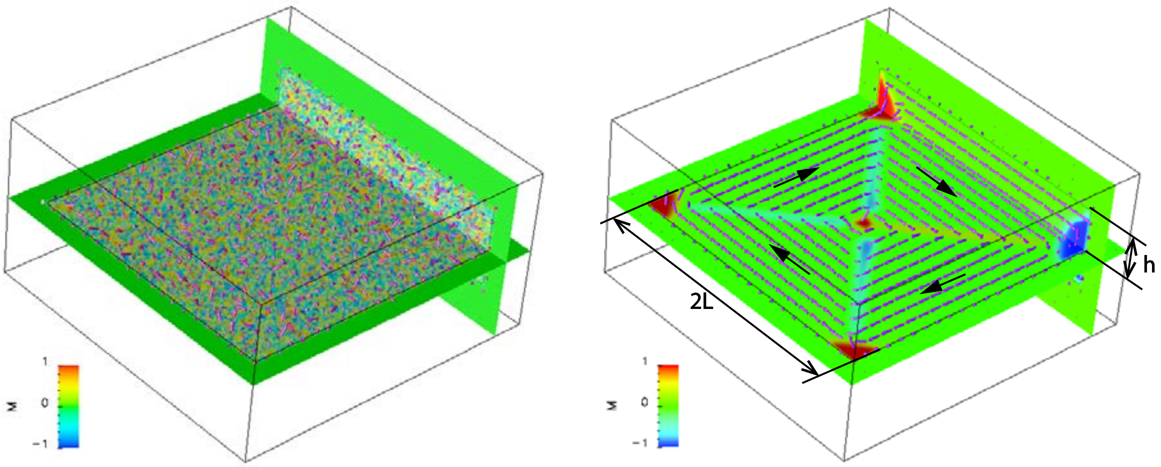

(a) (b)

Figure 3.1. Initial and Equilibrium Magnetic Domain Structures Obtained in a Free-standing α-Fe Film

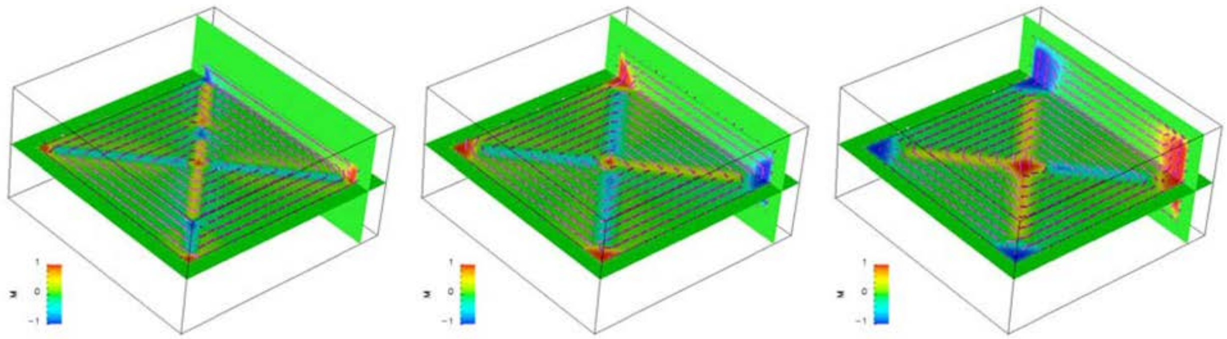

(a) 2h = 200 nm (b) 2h = 360 nm (c) 2h = 520 nm

Figure 3.2. Comparison of Film Thickness Effect on Ferromagnetic Domain Structures. The film in-plane size is 1120 nm × 1120 nm and thickness is 2h.

The simulation cell boundary is indicated by the black line box and of the size of $128l_0 \times 128l_0 \times 64l_0$ with $l_0 = 10$ nm for these square-shaped cells. The film size is 1120 nm × 1120 nm × 360 nm = 2L×2L×2h. The magnetic domain structure is illustrated by two cross sections of the film. One cross section is the middle section of the film. The other one is through the thickness of the film. The domain configuration is displayed in arrow plots. The arrows represent the magnetic vector magnitudes and directions. The black arrows show the direction of the magnetization vectors shown in the corresponding domains. The color represents the magnitude of the out-of-plane component, M_3^*, of the magnetic vector as indicated by the color bar.

Magnetic domain structure in a rectangular film is simulated in using a grid size of $96l_0 \times 192l_0 \times 64l_0$. The domain configuration depends on the film thickness and can be seen from Figure 3.3. The magnetization vector is still parallel to the film surface and forms a vortex shape with the head-to-tail magnetization configuration across a domain wall. But due to the unequal side lengths, there is more than one vortex in the thinner film. Again, the formations of these domain configurations are to reduce the magnetostatic energy and exchange energy. In a rectangular Fe specimen the simulation shows that two different domain wall configurations are possible. On the left side graph in Figure 3.3 (the 240 nm film) a long 180° domain wall exists, which are connected to the 90° walls at the corners of the rectangle. On the right-side graph in Figure 3.3 (the 120 nm film) there is no 180° wall and instead the vortices are connected by a diamond shape domain with 90° walls. Geometrically, both configurations are valid solutions, and the simulation predicts that the tendency towards one versus the other will be dictated by film thickness.

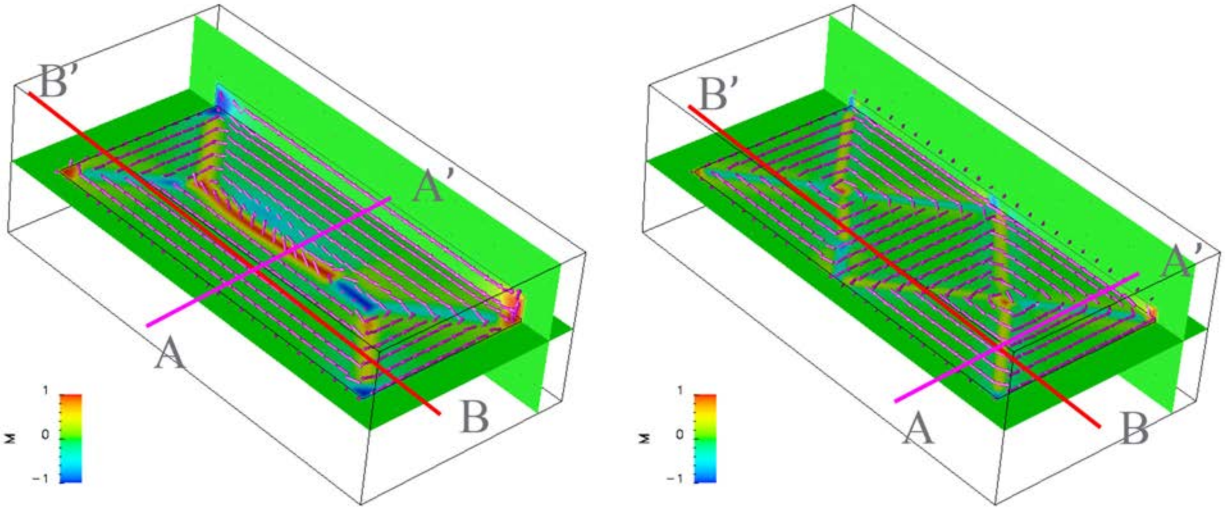

(a) 2h = 240 nm (b) 2h = 120 nm

Figure 3.3. Comparison of Film Size Effect on Magnetic Domain Structures. The in-plane size of the films is 800 nm × 1680 nm and thickness is 2h. The domain configuration is illustrated in arrow plots. The color represents the magnitude of the out-of-plane component, M_3^*, of the magnetic vector as indicated by the color bar.

3.2 Magnetic Domain Wall Thickness

Magnetization vector changes its direction across a domain wall. So domain wall thickness can be evaluated by checking the change of magnetization components. We have plotted the magnetization components along the lines AA' and BB' of Figure 3.3(a, b) and shown them in Figure 3.4(a–d). It is seen from Figure 3.4(a) that the 180° domain wall where M_1^* changes its value from 1 to −1 is about $6l_0 = 60$ nm as indicated the two dashed blue lines. Figure 3.4(b–d) all describe the 90° domain walls where M_1^* (M_2^*) changes its value from ±1 (0) to 0 (±1). They are all about $6l_0/\sqrt{2} \approx 42$ nm thick. The factor of $\sqrt{2}$ is due to the ~45° angle between the plotted lines and the 90° domain walls. A comparison with measured domain wall thicknesses from the MFM (Section 3.5) indicates that the computed values are significantly smaller than experimentally measured thicknesses (~500 nm-700 nm). This is likely due to the smaller domain sizes being modeled in the phase field model; this factor is being evaluated using larger domain sizes in the phase field models.

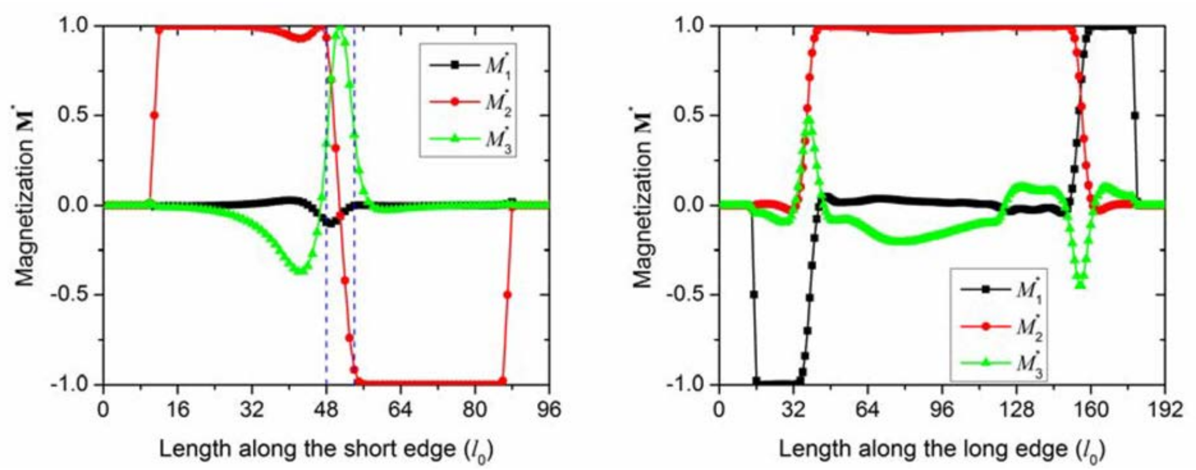

(a) Along line AA’ of Figure 3.3(a)　　(c) Along line BB’ of Figure 3.3(a)

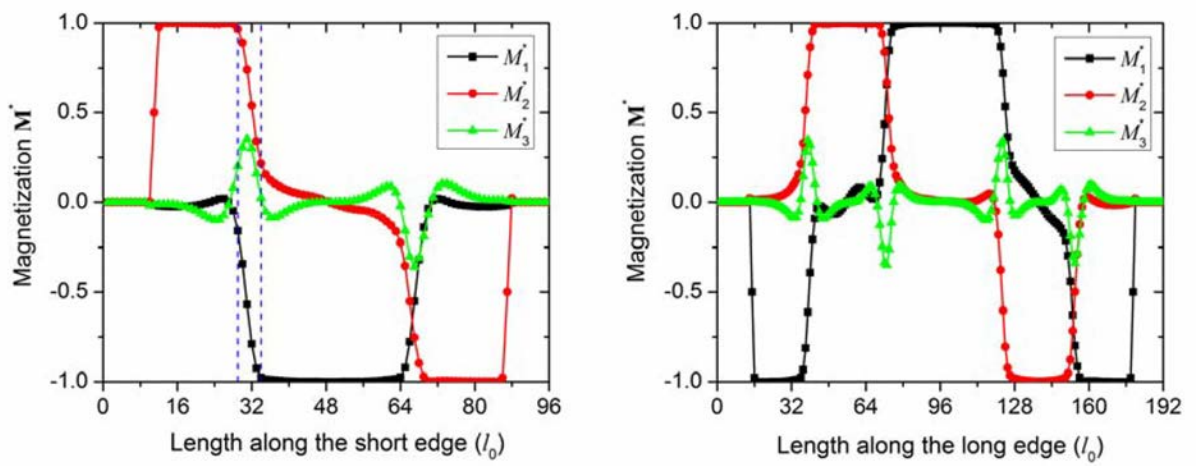

(c) Along line AA’ of Figure 3.3(b)　　(c) Along line BB’ of Figure 3.3(b)

Figure 3.4. Magnetization Varies Along the Lines AA’ and BB’ of Figure 3.3

3.3 Magnetic Domain Switching with Applied Magnetic Field

Without any applied magnetic field, the equilibrium magnetic domain structure will have zero average magnetization; that is, $\bar{\mathbf{M}} = \left(\bar{M}_1, \bar{M}_2, \bar{M}_3\right) = \left(0,0,0\right)$. Applying an external magnetic field can break this balance and alter the domain structure morphology. Figures 3.5 and 3.6 display the domain structure changes with applied field. In Figure 3.5, a magnetic field along the x_1-direction is applied to the domain structure shown in Figure 3.1(b). The applied filed is changing with time. The displayed domain morphologies from (a) to (e) are the snapshots when the applied field increased to the values (loading process) listed in the figure caption while (f) to (h) are the snapshots of the domain morphologies when the applied field decreased to the listed values (unloading process). The pairs of Figure 3.5(a) and (h), (b) and (g), (c) and (f) are, respectively, associated with the same values of the applied field but one is from the loading process and the other one is from the unloading process. The corresponding domain morphologies of each pair are similar to each other but not the exactly same. Actually, the domain morphology at the corresponding applied field depends on the loading rate; that is, the rate of the field increasing or decreasing. The $\Delta t = \Delta t^{*} t_0 = 0.1 t_0 = 0.26$ ps (picosecond) for each iteration and the loading rate is 10.3 kAm^{-1} per $2000\Delta t$ for Figure 3.5.

Figures 3.6 and -10 demonstrate the domain morphology change in loading process in rectangle films. Figure 3.6(a) is the same as Figure 3.3(a), which is the start point of the domain switching process. Similarly, Figure 3.7(a) is the same as Figure 3.3(b) as the starting point. Although the initial domain morphologies in the two rectangle films are different, the domain structures become similar to each other when the applied magnetic field is getting large. Both can be expected to be a single domain film when the applied field is big enough.

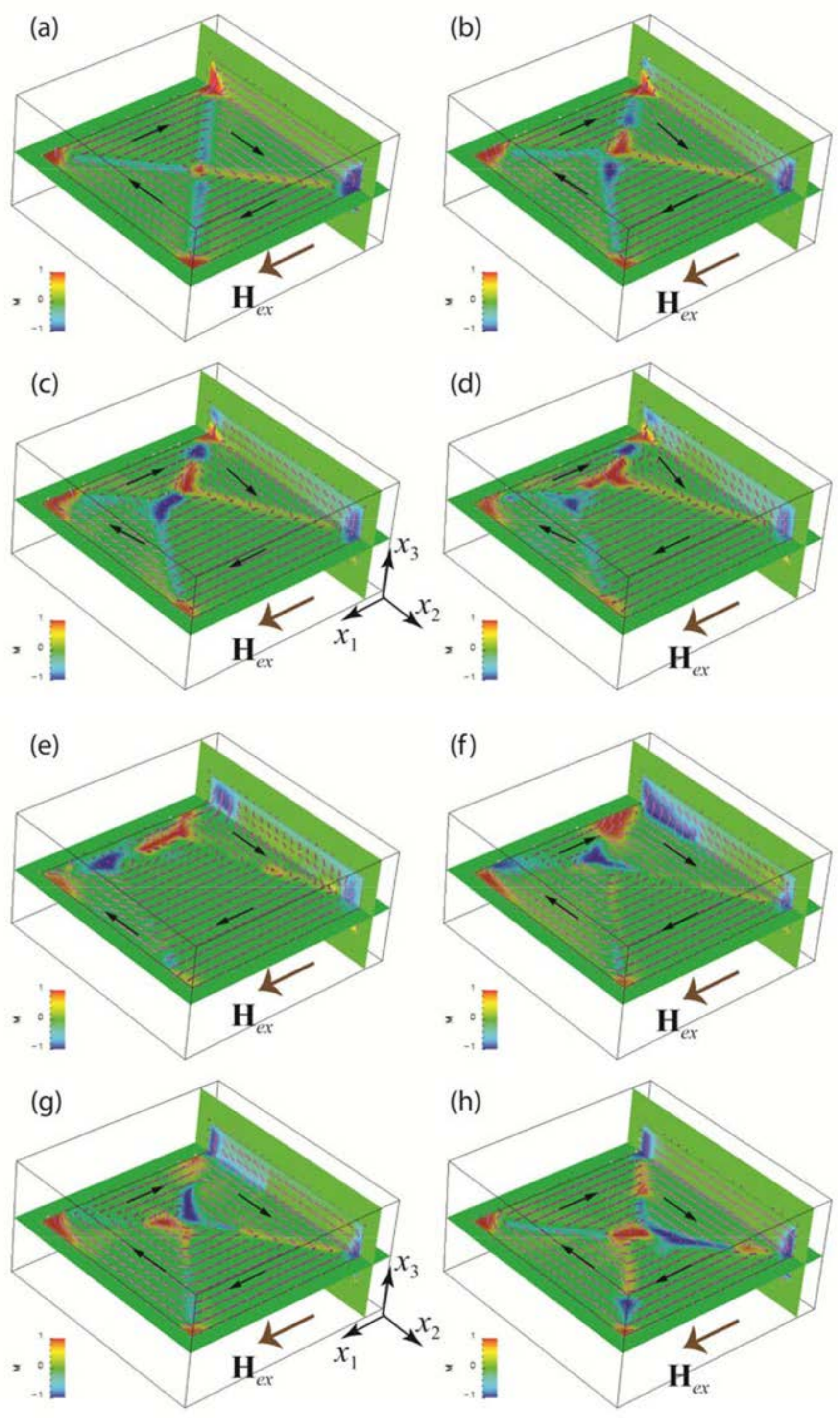

Figure 3.5. Magnetic Domain Switching with Applied Magnetic Field. (a) $\mathbf{H}_{ex} = (0,0,0)$; (b) $\mathbf{H}_{ex} = (40\times10^3,0,0)\mathrm{Am}^{-1}$; (c) $\mathbf{H}_{ex} = (60\times10^3,0,0)\mathrm{Am}^{-1}$; (d) $\mathbf{H}_{ex} = (80\times10^3,0,0)\mathrm{Am}^{-1}$; (e) $\mathbf{H}_{ex} = (100\times10^3,0,0)\mathrm{Am}^{-1}$; (f) $\mathbf{H}_{ex} = (60\times10^3,0,0)\mathrm{Am}^{-1}$; (g) $\mathbf{H}_{ex} = (40\times10^3,0,0)\mathrm{Am}^{-1}$; (h) $\mathbf{H}_{ex} = (0,0,0)$.

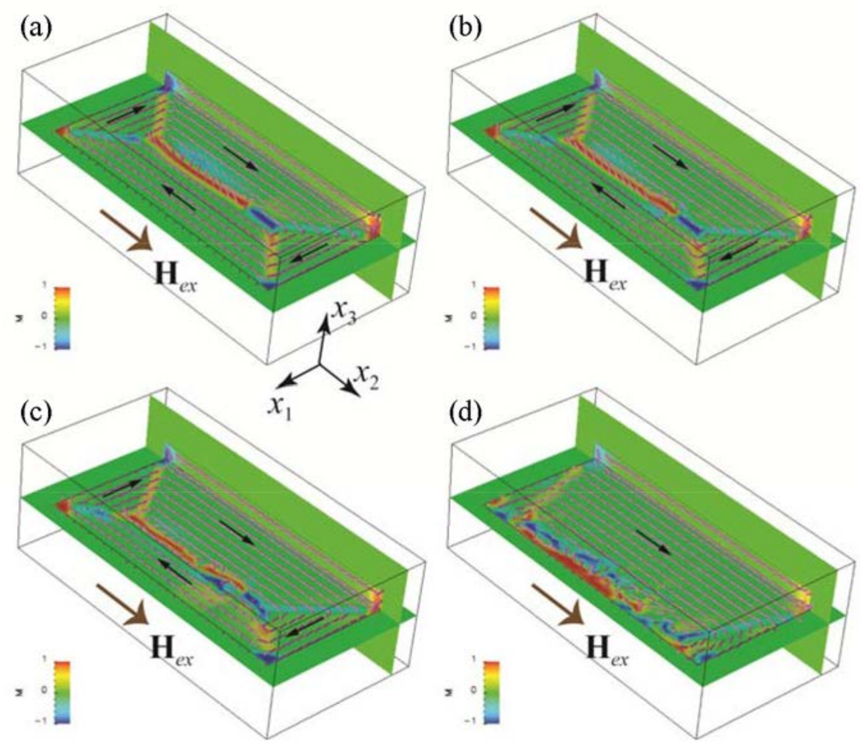

Figure 3.6. Magnetic Domain Switching with Applied Magnetic Field. (a) $\mathbf{H}_{ex} = (0,0,0)$; (b) $\mathbf{H}_{ex} = (0,18\times10^3,0)\mathrm{Am}^{-1}$; (c) $\mathbf{H}_{ex} = (0,30\times10^3,0)\mathrm{Am}^{-1}$; (d) $\mathbf{H}_{ex} = (0,84\times10^3,0)\mathrm{Am}^{-1}$.

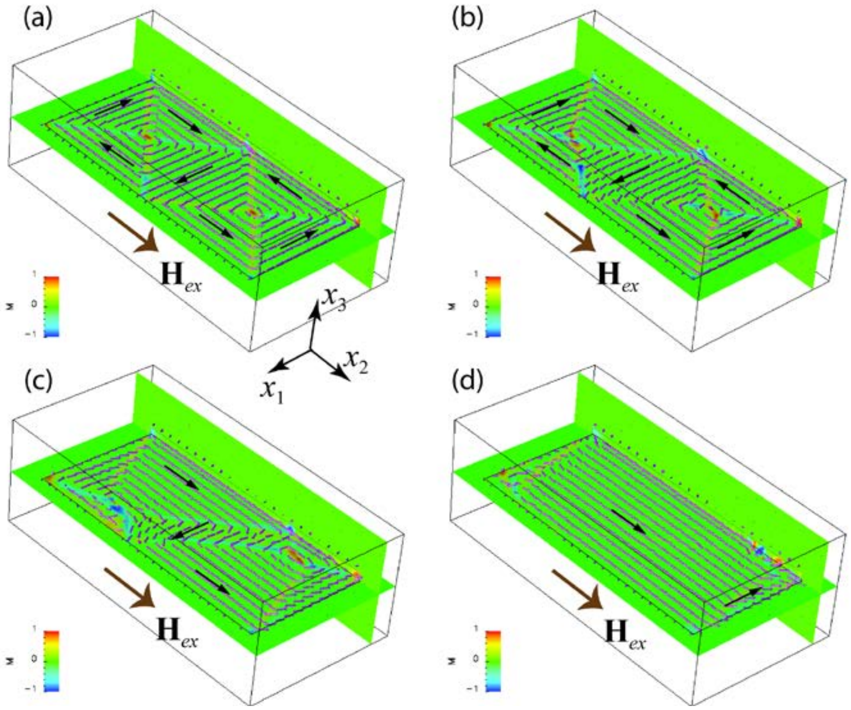

Figure 3.7. Magnetic Domain Switching with Applied Magnetic Field. (a) $\mathbf{H}_{ex} = (0,0,0)$; (b) $\mathbf{H}_{ex} = (0,19.2\times10^3,0)\text{Am}^{-1}$; (c) $\mathbf{H}_{ex} = (0,43.2\times10^3,0)\text{Am}^{-1}$; (d) $\mathbf{H}_{ex} = (0,67.2\times10^3,0)\text{Am}^{-1}$.

3.4 Experimental Set-up for MFM

Magnetic force microscopy images were obtained on an MFM with a variable field attachment (Asylum MFP-3D with VFM) providing the ability to induce an applied field of up to ±8,000 G. High coercivity tips with a 32-nm radius of curvature were chosen, representing a reasonable compromise between spatial resolution and magnetic field sensitivity. Generally speaking, MFM tips with higher field sensitivity tend to be coated with a thick metal layer (CoPt/FePt in this case), effectively blunting them (Schneider et al. 1996). The high coercivity tips (ASYMFMHC model, purchased from Asylum) proved ideal for this study because extremely high field sensitivity was not required and because their high coercivity (>5000 Oe) made it very unlikely that they would demagnetize from the fields applied to the Fe samples.

Focused ion beam milling was used to create small discrete shapes, essentially islands, in the single-crystal sample for the purpose of creating test areas with well-defined boundary conditions. Trenches approximately 1-µm deep were milled, through the Fe layers to assure complete penetration into the substrate, using an FEI Quanta dual-beam FIB tool. These trenches were 5-µm wide to magnetically isolate the shapes. Any degree of electromagnetic contact between the shapes and the surrounding layer would affect the domain walls in ways that would likely cause deviation from the computational model. FIB-milled shapes were 5 × 5 µm squares and 5 × 10 µm rectangles (Figure 3.8).

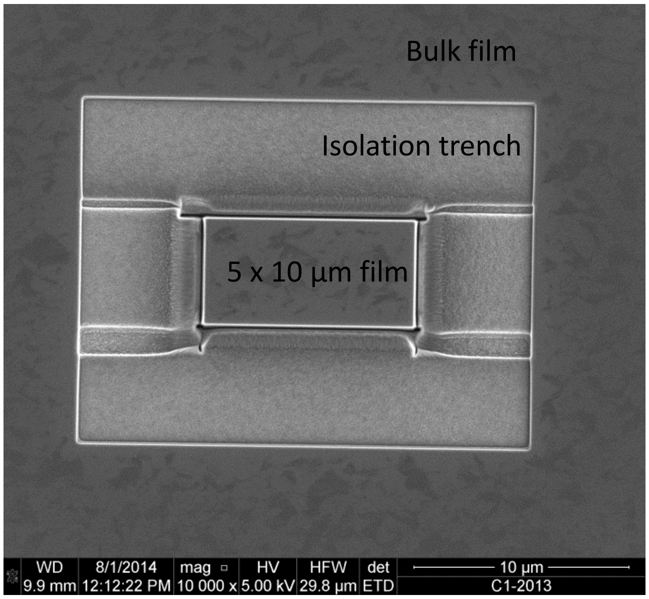

Figure 3.8. SEM Showing FIB-milled Rectangular "Island" in Single-crystal Fe Film

3.5 MFM and Modeling Comparisons for Single Crystal Film Fe

Figure 3.9 shows a series of MFM images taken at zero, positive, and negative fields for the rectangular FIB sample. The magnetization direction of each domain is depicted by the white arrow sitting in the domain, while the arrows underneath the images indicate the external magnetic field direction. Figure 3.9(a) and (d) show that the magnetic domain morphologies at zero applied field can be different. Figure 3.9(a) was from the initial moment before any magnetic field was applied while Figure 3.9(d) shows the domain wall configuration at zero applied field after the applied field was reduced to zero. The domain morphology in (a) is thermodynamically more stable than that in (d) because there are fewer domains, and thus less exchange energy. Thus the domain structure observed in (d) is metastable. It is observed because it takes time for the domain structure to fully relax. That is why the domain morphology in (d) can be obtained only during domain switching process where the domain structure has not completely reach its equilibrium state.

These experimental observations of domain wall configuration changes with applied field made with MFM were also able to be reproduced with our phase field computational models. For example, the movement and shrinkage of the "diamond" section in the middle of the specimen is similar to the behavior predicted in Figure 3.7 and exhibits great symmetry [see (c) and (e)] with positive and negative field. The same features of different domain morphologies at zero applied field measured with the MFM in Fig. 3.9 were also obtained from our phase field model simulations as displayed in Figure 3.10. Exact domain structures were captured before applying any field and when the field reduces to zero during switching. Further corroboration between modeling and measurements on a square shaped specimen is shown in Fig. 3.11. This high level of agreement between MFM measurements and computational simulations of magnetic domain wall structures is excellent confirmation that our models are able to produce reasonable simulations of basic magnetic behavior in thin, defect-free, Fe films.

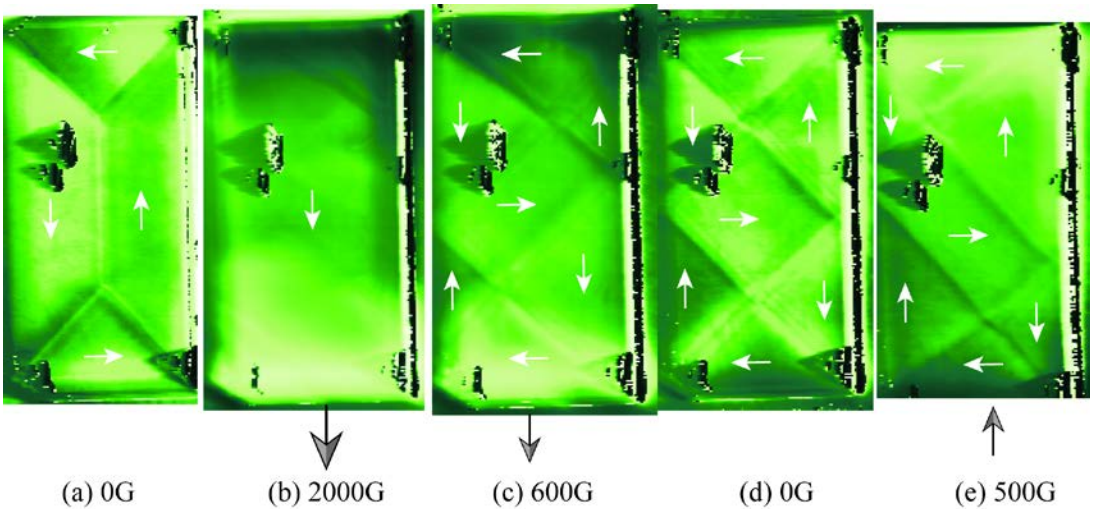

Figure 3.9. MFM Images as a Function of Applied Field for the 5 × 10 µm FIB Region of Single Crystal Fe. The arrows on the images represent the magnetization vector directions of the domains. The arrows below the images refer to the directions of the applied magnetic field. The numbers are the magnitudes of the applied magnetic field. . (a) initial domain structure before applying field; (b) domain structure at the maximum applied field; (c) domain structure at the moment when applied field reduces to the given field from the maximum; (d) domain structure when applied field reduces to zero; (e) domain structure at the moment when applied field increase to the given field from zero.

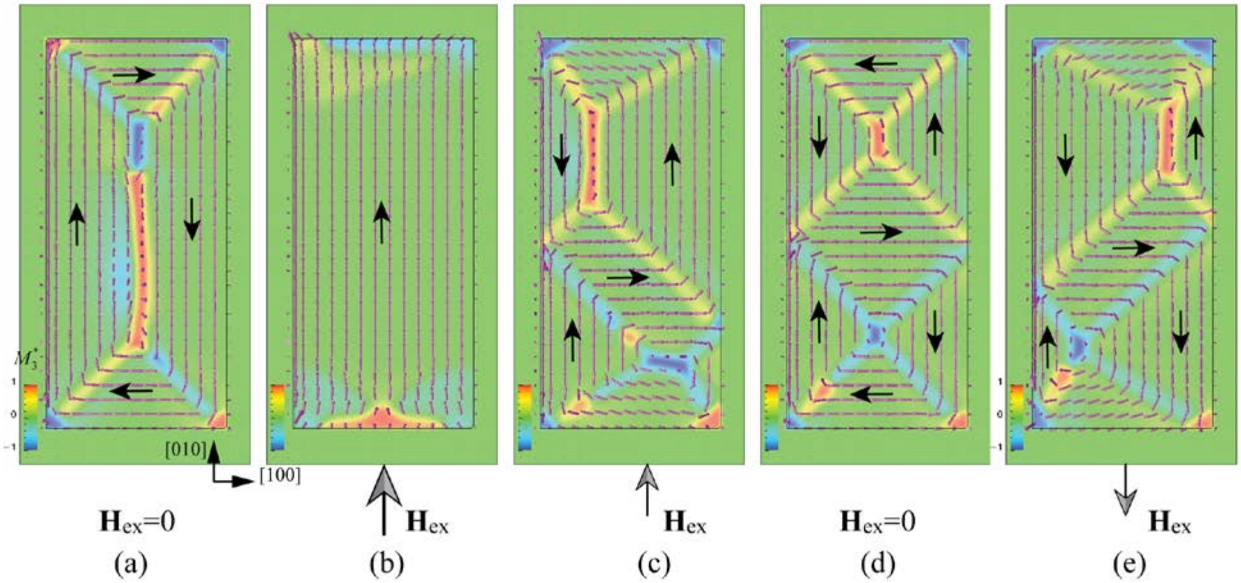

Figure 3.10. Phase-Field Simulation of Rectangular Aspect Ratio Fe Films during Domain Switching. The film thickness is 240 nm. The arrows (both small and magnified) in the images represent the magnetization vector directions and magnitude. The color represents the magnitude of

the component M_3^* of the magnetization vector as indicated by the color bar. The arrows underneath the images refer to the directions and magnitude of the applied magnetic field. . (a) initial domain structure before applying field; (b) domain structure at the maximum applied field; (c) domain structure at the moment when applied field reduces to the given field from the maximum; (d) domain structure at the moment when applied field reduces to zero the given field from the maximum;; (e) domain structure at the moment when applied field increase to the given field from zero.

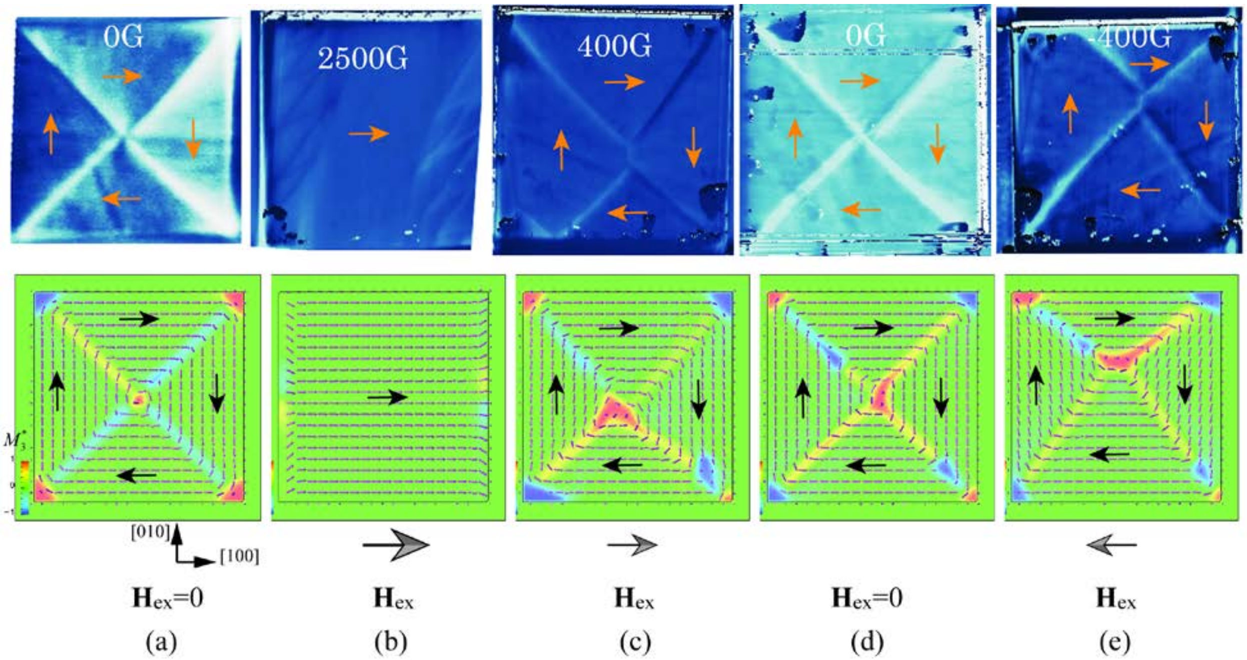

Figure 3.11. Comparison between Phase-Field Simulation (bottom row) and MFM Measurements (top row) of Square Aspect Ratio Fe Thin Film during Domain Switching. The arrows on the domains are corresponding to the magnetization vector directions of the domains. The color represents the magnitude of the component M_3^* of the magnetization vector as indicated by the color bar. The arrows underneath the images refer to the applied field directions. (a) initial domain structure before applying field; (b) domain structure at the maximum applied field; (c) domain structure at the moment when applied field reduces to the given field from the maximum; (d) domain structure when applied field reduces to zero; (e) domain structure at the moment when applied field increase to the given field from zero.

3.6 MFM of Polycrystalline Film Fe

EBSD and MFM were performed on the polycrystalline iron film on polycrystalline MgO substrate. An example of a sub-region showing the comparison of crystallographic and magnetic information is shown in Figure 3.12. A sub-region of this film was scribed in a 100-µm square so comparable regions could be located. Sub-areas of this scribed region were investigated with field-dependent MFM, as shown in Figure 3.13, and movies were created to visualize movement of domain walls in the presence of grain boundaries. Preliminary findings of MFM versus applied field indicate that domain walls can stop at grain boundaries or go through them, depending on the boundary, indicating a possible magneto-crystalline (i.e., crystallographic orientation) component to the domain wall mobility. Additionally, some grain boundaries nucleated spike domains, an important consideration for magnetization reversal mechanisms. Future work will involve FIB of individual features of this polycrystalline sample, including single grain boundaries and triple points, to further investigate the effect of crystallographic differences in domain wall motion.

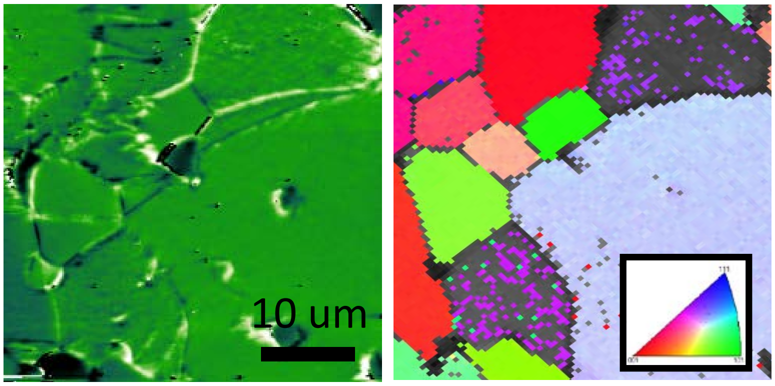

Figure 3.12. MFM (left) and Corresponding EBSD (right) Image of Thin Film Polycrystalline Fe at the Same Scale (40-µm square field of view). Microstructural features can be correlated between the two images.

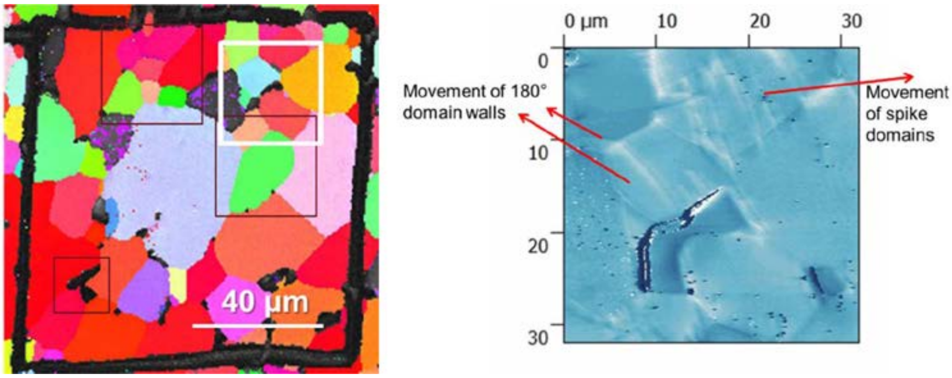

Figure 3.13. EBSD Image (left) of Portion of the Polycrystalline Iron Film, with the Large Black Square Indicating the ~100-µm Scribed Area (note, not FIB'd). Smaller squares indicate different regions that were examined using field-dependent MFM, with the one outlined in white being the region indicated by the MFM shown (right).

4.0 Conclusions and Future Work

This report presents progress towards the development of meso-scale models of magnetic behavior that incorporate microstructural information. The research is part of a greater effort to integrate microstructural metrology, micro-magnetic measurements, and meso-scale phase-field modeling to develop advanced tools and techniques that can extract semi-quantitative diagnostic and interpretive information about the state of microstructural damage in a material based on magnetic signature data alone.

The focus of the modeling is on phase-field models. The models are based on the numerical solution to the Landau-Lifshitz-Gilbert equation; the numerical solution uses a modified fast Fourier transform algorithm. From the computational standpoint, phase-field modeling allows the simulation of large enough systems that relevant defect structures and their effects on functional properties like magnetism can be simulated. In particular, phase-field models of magnetic domain evolution enable the study of the effect of individual defects, such as magnetic particles and dislocations on magnetic domain nucleation, DW mobility, and magnetic response.

Two phase-field models have been generated in support of this work. First, a bulk iron model with periodic boundary conditions was generated as a proof-of-concept to investigate major loop effects of single versus polycrystalline bulk iron and effects of single non-magnetic defects. This model can be implemented using parallel processing. Additionally, a new model was generated that uses finite boundary conditions representing surfaces and edges. This model can be used to simulate the magnetic behavior of thin films and is implemented in a serial fashion. It uses a grid size of 128×128×64 or 96×192×64. Based on a grid spacing of 10 nm, the thin models represent physical dimensions of 1280 nm × 1280 nm × 640 nm, or 960 nm × 192 nm × 64 nm. The simulations are based on material parameters for BCC α-phase iron, to enable comparisons with measurements on iron thin-films.

Thin film model simulations were verified using an MFM to measure magnetic domain wall structures and their motion as a function of applied field. Measurements were made on single crystal, thin-film Fe specimens that were 5 µm × 10 µm × 250-nm thick. An SEM FIB was used to fabricate the test specimens. Comparisons between phase-field model simulations and MFM measurements show several important results:

1. Phase-field models for zero magnetic field DW structures have been qualitatively verified for square and rectangular structures.
2. Phase-field models for changes in DW motion with changes in applied magnetic field have been qualitatively verified for rectangular structures.
3. Phase-field model results were able to explain the observed differences in zero magnetic field DW structures in rectangular specimens (e.g., Figure 3.10 – the presence of 180° DWs and 90° DWs) as being the result of a thin specimen that was close to a critical thickness.

Ongoing research is focused on validation of the phase-field model. Validation is expected to be through continued comparison with experimentally obtained MFM images. Additionally, we plan to make measurements of major hysteresis loops and FORC curves using VSM and compare those results to the phase-field model predictions as well. Extrapolation of simulation sizes to represent a more stochastic bulk-like system will require sampling of various simulations (i.e., with single non-magnetic defect, single magnetic defect, single grain boundary, single dislocation, etc.) with distributions of input parameters. These outputs can then be compared to laboratory magnetic measurements and ultimately to simulated magnetic Barkhausen noise signals.

Future work will focus on the following:

- Quantitative comparison between phase-field models and MFM results for changes in DW motion with applied magnetic field and DW thickness. To enable this, phase-field model size will be increased and FIB specimen size will be decreased so that both the model and the measurements will be at the same dimensions (e.g., 2 μm × 4 μm, and 200 × 400 nodes).
- Additional complexity will be added to the model and appropriate specimens will be fabricated to verify model results:
    a. Single void in a rectangular single crystal Fe thin film specimen
    b. Rectangular specimens aligned to different crystallographic axes
    c. Diamond shaped specimen that is 45° to a principal crystallographic axis
    d. Grain boundary parallel to the long axis of a rectangular specimen
    e. Grain boundary perpendicular to the long axis of a rectangular specimen
- Comparisons between phase-field model simulations and VSM and FORC measurements will be made to verify the ability of the models to predict magnetic hysteresis behavior.

In summary, thin film phase-field models have been built, specimens of similar size to the phase-field models have been fabricated from single crystal, thin-film iron specimens using a FIB. Model simulations of magnetic behavior were verified with MFM measurements. Unexpected variations in MFM measurements could be explained using the phase-field model to simulate the effect of differences in specimen thickness. These results are very promising, and we are optimistic that future growth of the project will continue to yield valuable outcomes.

5.0 References

Adams JJ, DS Agosta, RG Leisure and H Ledbetter. 2006. "Elastic Constants of Monocrystal Iron from 3 to 500 K." *Journal of Applied Physics* 100(11):113530 - 113530-7.

Altpeter I, G Dobmann, KH Katerbau, M Schick, P Binkele, P Kizler and S Schmauder. 2001. "Copper Precipitates in 15 NiCuMoNb 5 (WB 36) Steel: Material Properties and Microstructure, Atomistic Simulation, and Micromagnetic NDE Techniques." *Nuclear Engineering and Design* 206(2-3):337-350.

Babcock KL, VB Elings, J Shi, DD Awschalom and M Dugas. 1996. "Field-dependence of Microscopic Probes in Magnetic Force Microscopy." *Applied Physics Letters* 69(5):705-707.

Batista L, U Rabe and S Hirsekorn. 2012. "Micro- and Nanostructure Characterization and Imaging of TWIP and Unalloyed Steels." In *Proceedings of 38th Annual Review of Progress in Quantitative Nondestructive Evaluation*, pp. 1381-1388. July 17-22, 2011, Burlington, Vermont. American Institute of Physics, Melville, New York. AIP Vol. 1430.

Batista L, U Rabe and S Hirsekorn. 2013. "Magnetic Micro- and Nanostructures of Unalloyed Steels: Domain Wall Interactions with Cementite Precipitates Observed by MFM." *NDT & E International* 57:58-68.

Bertotti G. 1998. *Hysteresis in Magnetism: for Physicists, Materials Scientists, and Engineers*. Academic Press, San Diego. ISBN 0120932709, 9780120932702.

Chang K-O, S-H Chi, K-J Choi, B-C Kim and S-L Lee. 2002. "Changes in Magnetic Parameters of Neutron Irradiated RPV Linde80 High Copper Weld Surveillance Specimens." *International Journal of Pressure Vessels and Piping* 79(11):753-757.

Craik D. 1995. *Magnetism: Principles and Applications*. John Wiley & Sons, Chichester.

Cullity BD and CD Graham. 2009. *Introduction to Magnetic Materials*. Wiley & IEEE Press.

d'Aquino M. 2004. *Nonlinear Magnetization Dynamics in Thin-films and Nanoparticles*. Ph.D Thesis, Universita degli studi di Napoli Federico II, Italy.

Gilbert TL. 2004. "A Phenomenological Theory of Damping in Ferromagnetic Materials." *IEEE Transactions on Magnetics* 40(6):3443-3449.

Gussev MN, JT Busby, L Tan and FA Garner. 2014. "Magnetic Phase Formation in Irradiated Austenitic Alloys." *Journal of Nuclear Materials* 448(1–3):294-300.

Henager Jr. CH, JS McCloy, P Ramuhalli, DJ Edwards, S Hu and Y Li. 2013. "Investigation of Magnetic Signatures and Microstructures for Heat-treated Ferritic/Martensitic HT-9 Alloy." *Acta Materialia* 61(9):3285-3296.

Hu SY, YL Li, J McCloy, R Montgomery and CH Henager. 2013. "Magnetic Hardening from the Suppression of Domain Walls by Nonmagnetic Particles." *IEEE Magnetics Letters* 4:3500104

Hubert A and R Schaefer. 1998. *Magnetic Domain: The Analysis of Magnetic Microstructures*. Springer, Berlin.

Kamada Y, H Watanabe, S Mitani, JN Mohapatra, H Kikuchi, S Kobayashi, M Mizuguchi and K Takanashi. 2013. "Ion-irradiation Enhancement of Materials Degradation in Fe–Cr Single Crystals Detected by Magnetic Technique." *Journal of Nuclear Materials* 442(1-3, Suppl 1):S861-S864.

Kempf RA, J Sacanell, J Milano, N Guerra Méndez, E Winkler, A Butera, H Troiani, ME Saleta and AM Fortis. 2014. "Correlation between Radiation Damage and Magnetic Properties in Reactor Vessel Steels." *Journal of Nuclear Materials* 445(1–3):57-62.

Kobayashi S, H Kikuchi, S Takahashi, Y Kamada, K Ara, T Yamamoto, D Klingensmith and GR Odette. 2009. "The Effect of Copper and Manganese on Magnetic Minor Hysteresis Loops in Neutron Irradiated Fe Model Alloys." *Journal of Nuclear Materials* 384(2):109-114.

Kobayashi S, S Tsukidate, Y Kamada, H Kikuchi and T Ohtani. 2012a. "Investigation of Scaling Laws in Frequency-dependent Minor Hysteresis Loops for Ferromagnetic Steels." *Journal of Magnetism and Magnetic Materials* 324(2):215-221.

Kobayashi S, T Yamamoto, D Klingensmith, GR Odette, H Kikuchi and Y Kamada. 2012b. "Magnetic Evaluation of Irradiation Hardening in A533B Reactor Pressure Vessel Steels: Magnetic Hysteresis Measurements and the Model Analysis." *Journal of Nuclear Materials* 422(1–3):158-162.

Lau JW and JM Shaw. 2011. "Magnetic Nanostructures for Advanced Technologies: Fabrication, Metrology and Challenges." *Journal of Physics D: Applied Physics* 44(30):303001.

Lo CCH. 2012. "Effects of Copper Precipitation on the Magnetic Properties of Aged Copper-containing Ferrous Alloys." In *Proceedings of 38th Annual Review of Progress in Quantitative Nondestructive Evaluation*, pp. 1351-1358. July 17-22, 2011, Burlington, Vermont. DOI doi:http://dx.doi.org/10.1063/1.4716374. American Institute of Physics, Melville, New York. AIP Vol. 1430.

Mayergoyz ID. 1991. *Mathematical Models of Hysteresis*. Springer-Verlag, New York.

McCloy JS, P Ramuhalli and JC Henager. 2013. "Use of First Order Reversal Curve Measurements to Understand Barkhausen Noise Emission in Nuclear Steel." In *Review of Progress in Quantitative Nondestructive Evaluation, Vol. 32*, pp. 1709-1716 Denver, Colorado. DOI 10.1063/1.4789247. American Institute of Physics, Mellville, New York.

Newell AJ. 2005. "A high-precision model of first-order reversal curve (FORC) functions for single-domain ferromagnets with uniaxial anisotropy." *Geochem. Geophys. Geosyst.* 6(5):Q05010.

Park D-G, J-H Hong, I-S Kim and H Kim. 1997. "Evaluation of Thermal Recovery of Neutron-irradiated SA508-3 Steel Using Magnetic Property Measurements." *Journal of Materials Science* 32(23):6141-6146.

Park D-G, H-T Jeong and J-H Hong. 1999a. "Study on the Radiation Damage and Recovery of Neutron Irradiated Vessel Steel Using Magnetic Barkhausen Noise." *Journal of Applied Physics* 85:5726-5728.

Park DG, EJ Moon, DJ Kim, SH Chi and JH Hong. 2003. "The Change of Saturation Magnetization in Neutron-irradiated Low-alloy Steel." *Physica B: Condensed Matter* 327(2-4):315-318.

Park DG, CI Ok, HT Jeong, IH Kuk and JH Hong. 1999b. "Nondestructive Evaluation of Irradiation Effects in RPV Steel Using Barkhausen Noise and Magnetoacoustic Emission Signals." *Journal of Magnetism and Magnetic Materials* 196:382-384.

Park DG, S-S Park, K-O Chang and J-H Hong. 2004. "The Change of Magnetic Relaxation in Neutron Irradiated Ni–Cr–Mo Steel." *Physica Status Solidi (b)* 241(7):1621-1624.

Ramuhalli P, CH Henager Jr, JW Griffin, RM Meyer, JB Coble, SG Pitman and LJ Bond. 2012. "Material Aging, Degradation Detection and Remaining Life Assessment for Plant Life Management." In *3rd International Conference on NPP Life Management (PLIM) for Long Term Operations (LTO)*. May 13-17, 2012, Salt Lake City, Utah. International Atomic Energy Agency, Vienna, Austria.

Schneider M, S Müller-Pfeiffer and W Zinn. 1996. "Magnetic Force Microscopy of Domain Wall Fine Structures in Iron Films." *Journal of Applied Physics* 79(11):8578-8583.

Sipahi LB, MR Govindaraju and DC Jiles. 1994. "Monitoring Neutron Embrittlement in Nuclear Pressure Vessel Steels using Micromagnetic Barkhausen Emissions." *Journal of Applied Physics* 75(10):6981-6983.

Sorop TG, C Untiedt, F Luis, M Kröll, M Raşa and LJ de Jongh. 2003. "Magnetization Reversal of Ferromagnetic Nanowires Dtudied by Magnetic Force Microscopy." *Physical Review B* 67(1):014402.

Takahashi S, H Kikuchi, K Ara, N Ebine, Y Kamada, S Kobayashi and M Suzuki. 2006. "In Situ Magnetic Measurements Under Neutron Radiation in Fe Metal and Low Carbon Steel." *Journal of Applied Physics* 100(2):023902.

Takaya S, T Suzuki, Y Matsumoto, K Demachi and M Uesaka. 2004. "Estimation of Stress Corrosion Cracking Sensitivity of Type 304 Stainless Steel by Magnetic Force Microscope." *Journal of Nuclear Materials* 327(1):19-26.

Wang XP, CJ Garcia-Cervera and WN E. 2001. "A Gauss-Seidel Projection Method for Micromagnetics Simulations." *Journal of Computational Physics* 171:357-372.

Winklhofer M and GT Zimanyi. 2006. "Extracting the Intrinsic Switching Field Distribution in Perpendicular Media: A Comparative Analysis." *Journal of Applied Physics* 99(8):08E710-08E710-3.

Zhang JX and LQ Chen. 2005. "Phase-field Microelasticity Theory and Micromagnetic Simulations of Domain Structures in Giant Magnetostrictive Materials." *Acta Materialia* 53(9):2845-2855.

Zhu X, P Grutter, V Metlushko, Y Hao, FJ Castano, CA Ross, B Ilic and HI Smith. 2003. "Construction of Hysteresis Loops of Single Domain Elements and Coupled Permalloy Ring Arrays by Magnetic Force Microscopy." *Journal of Applied Physics* 93(10):8540-8542.

Zinkle SJ and JT Busby. 2009. "Structural Materials for Fission & Fusion Energy." *Materials Today* 12(11):12-19.

www.pnnl.gov

Pacific Northwest
NATIONAL LABORATORY

Proudly Operated by Battelle Since 1965

U.S. DEPARTMENT OF
ENERGY

902 Battelle Boulevard
P.O. Box 999
Richland, WA 99352
1-888-375-PNNL (7665)